Nucleation kinetics during homoepitaxial growth of TiN(001) by reactive magnetron sputtering

Marcel A. Wall, David G. Cahill, I. Petrov, D. Gall, and J. E. Greene
Department of Materials Science and the Frederick Seitz Materials Research Laboratory, University of Illinois, 104 South Goodwin Avenue, Urbana, Illinois 61801, USA
(Received 22 July 2003; published 21 July 2004)

We use scanning tunneling microscopy to study the nucleation of homoepitaxial TiN layers grown on TiN(001) by ultrahigh vacuum reactive magnetron sputtering in pure N_2. Nucleation lengths are measured using *in situ* scanning tunneling microscopy as a function of temperature on two-dimensional islands as well as on large open terraces. At low growth temperatures, $500 \leqslant T_s \leqslant 865\ °C$, nucleation is diffusion limited and we extract a surface diffusion energy of 1.4 ± 0.1 eV. At higher temperatures, $865 \leqslant T_s \leqslant 1010\ °C$, nucleation is limited by the formation rate of stable clusters for which we obtain an activation energy of 2.6 ± 0.2 eV. *Ab initio* calculations combined with our experimental results suggest that the primary diffusing adspecies are TiN_x molecules with $x=2$ and/or 3.

DOI: 10.1103/PhysRevB.70.035413 PACS number(s): 68.55.Ac

I. INTRODUCTION

Understanding nucleation and early stage growth is central to relating film deposition parameters to the texture and surface morphology of as-deposited polycrystalline layers. Progress in experiment and theory have led to improved understanding of the kinetics which govern these processes.[1–8] However, the majority of the studies have been carried out for elemental metals and semiconductors. We use scanning tunneling microscopy (STM) to investigate nucleation kinetics of TiN, a two-component refractory ceramic, on TiN(001).

TiN, typically deposited by reactive magnetron sputtering, is widely used in a variety of applications including hard wear-resistant coatings on cutting tools,[9] corrosion-resistant coatings,[10] scratch resistant and antireflective layers on optical components,[11] and diffusion barriers in microelectronics.[12] In all cases, coating performance is strongly affected by surface roughness and film texture,[13,14] both of which are largely determined by surface diffusion and nucleation kinetics during the early stages of film growth.[14–16] Thus, an understanding of these processes is important for controlling the growth and properties of polycrystalline TiN layers.

Walton[3] developed a thermodynamic model to predict the density of unstable clusters during film growth as a function of temperature and the adatom concentration on a terrace whose width d is large compared to the nucleation length L_n, i.e., the characteristic separation between stable islands. Venables[4] incorporated Walton's model into a rate equation formalism that predicts the nucleation length as a function of the adatom diffusivity and the binding energy of unstable clusters.

An expression describing the characteristic island size necessary to nucleate a new layer on a growing two-dimensional (2D) island as a function of adatom diffusivity was developed by Stoyanov and Markov[1] based upon rate equation theory. Tersoff *et al.*[2] extended the model to include asymmetry in the adatom attachment rates at the edge of the growing island. Adatom attachment asymmetry at ascending versus descending steps is often termed the Ehrlich barrier.[17]

We grow epitaxial TiN layers on TiN(001) via reactive magnetron sputtering in a multichamber ultra-high vacuum (UHV) system and use *in situ* scanning tunneling microscopy (STM) to investigate nucleation kinetics over a wide temperature range on large atomically flat terraces as well as on growing islands. The use of both approaches extends the temperature range over which nucleation can be studied on TiN(001). Nucleation lengths are measured on large terraces at $500 \leqslant T_s \leqslant 800\ °C$ and on growing islands at $650 \leqslant T_s \leqslant 1010\ °C$. By combining experiment and theory, we extract a diffusion activation energy of 1.4 ± 0.1 eV for diffusion limited nucleation and an activation energy of 2.6 ± 0.2 eV when nucleation is limited by the formation of stable clusters.

In order to interpret the experimental results, we carry out *ab initio* density functional theory (DFT) calculations of the adsorption, binding, and diffusion activation energies for adatoms and small TiN admolecules on TiN(001). The calculations provide insight into the rate-limiting atomistic processes occurring on the surface during TiN film growth.

II. EXPERIMENTAL PROCEDURE

TiN(001) layers are grown in a load-locked multichamber UHV magnetron sputter deposition system which has a base pressure of 10^{-10} Torr.[18,19] A high purity (99.999%) 7.5-cm-diameter Ti disc is sputtered in an atmosphere of purified N_2 at a pressure of 3 mTorr with a target-to-substrate distance of 20 cm. We use a constant power of 375 W, resulting in a Ti atom deposition rate of 1.6 atoms/nm^2 s as determined, and periodically confirmed, by Rutherford backscattering spectrometry and x-ray reflectivity measurements.

The substrates are polished $10 \times 10 \times 0.5\ mm^3$ NaCl-structure MgO(001) wafers. MgO is isostructural with TiN and has a lattice parameter mismatch of only 0.006 at room temperature and $\simeq 0.001$ at the deposition temperatures, $500 \leqslant T_s \leqslant 1010\ °C$, used in these experiments. The MgO(001) substrates are first annealed in air at 1400 °C for 4 h in order to provide atomically flat terraces which are

 ©2004 The American Physical Society

$\simeq$1 μm wide as determined by atomic force microscopy (AFM). The AFM measurements are carried out in air with oxide-sharpened Si_3N_4 tips. The images are linearly planarized to remove sample tilting effects which occurred during the measurements.

Following annealing, a 300-nm-thick Mo layer is sputter deposited on the back of each substrate to enable temperature measurement using an infrared pyrometer operated at wavelengths $\lambda=1-1.5$ μm, for which MgO is transparent. The emissivity ε of TiN was determined using ellipsometry at temperatures between 23 and 400 °C yielding $\varepsilon=[0.0758+1.09\times10^{-4}T_s]$ (with T_s expressed in °C) for $\lambda=1.3$ μm and $\varepsilon=[0.224+1.88\times10^{-4}T_s]$ at $\lambda=0.650$ μm. The emissivity results are linearly extrapolated to the film growth temperatures and reduced by 10% to account for reflections from the glass viewport. Infrared pyrometer ($\lambda=1.3$ μm) temperature measurements agree, to within an uncertainty of less than 2%, with T_s values obtained using a disappearing filament pyrometer ($\lambda=0.650$ μm).

The substrate and sample block are degassed in the growth chamber for 1 h at 1050 °C. An initial 20-nm-thick epitaxial TiN(001) buffer layer is then grown at 650 °C in order to bury any residual impurities at the substrate surface. This is followed by the growth of a second TiN(001) layer, 40-nm-thick, at $T_s=750$ °C. The latter temperature was chosen since it was previously shown, using the same deposition conditions and growth chamber, to result in the lowest reported room temperature resistivity $\rho_{300}=13$ $\mu\Omega$ cm for either bulk or thin film TiN.[18–20] The buffer layers provide a consistent source of black-body radiation for measuring T_s and serve as the homoepitaxial substrate for our nucleation experiments.

To obtain large, $\simeq$60-nm-wide, TiN(001) terraces for nucleation studies, we deposit an additional 8-nm-thick layer at $T_s=1050$ °C. The sample temperature is then adjusted over a period of <2 min to the value $T_s=500-800$ °C chosen for the terrace nucleation experiment and 0.5 ML of TiN is deposited. The sample is allowed to cool to room temperature and transferred *in situ* to the STM chamber for imaging. Typical tunneling conditions are a current of 0.25 nA with a bias of +1 V.

We also study nucleation on growing islands in order to confirm the validity of applying existing nucleation theories to a two-component system and to extend the temperature range of our measurements. In this case, the deposition sequence is initiated with the two-step buffer layer described above. T_s is then adjusted to the temperature chosen for the experiment and an 8-nm-thick TiN(001) layer is grown. The sample is cooled to room-temperature and transferred to the STM chamber for imaging.

The epitaxial nature of the TiN(001) layers is confirmed using ω-2θ and ϕ-scan x-ray diffraction (XRD). The ω-2θ measurements are carried out in a high-resolution diffractometer with Ge(220) four-crystal and two-crystal monochromators in the primary and secondary x-ray axes, respectively. With Cu $K_{\alpha1}$ radiation ($\lambda=0.15$ 405 nm), this arrangement provides an angular beam divergence of $\simeq$12 arc s with a wavelength spread of $\Delta\lambda/\lambda\simeq7\times10^{-5}$. The ϕ-scans are obtained using a four-circle Phillips MRD diffractometer with parallel-beam x-ray optics, a 1×1 mm^2 point-focus Cu x-ray source with a Ni filter, and a 1×1 mm^2 collimator slit at a distance of 160 mm from the source. This configuration results in a 0.35° divergence of the incident beam. The secondary optics in the ϕ-scan configuration consist of a 0.27° parallel-plate collimator, a flat graphite secondary monochromator, and a proportional detector.

The purity, stoichiometry, and crystalline quality of as-deposited TiN(001) layers are confirmed by temperature-dependant resistivity measurements. An in-line four-point probe is used to determine the room-temperature resistivity ρ_{300K}, while temperature-dependant measurements are carried out between 20 and 300 K in a temperature-controlled vacuum cryostat.

III. COMPUTATIONAL METHODS

We use density functional theory to calculate the binding energies E_b, adsorption energies E_{ad}, and diffusion activation barriers E_s for N_2, N, and TiN_x ($x=0,1,2,3,4$) adspecies on TiN(001).[21] The calculations are carried out using the Vienna *ab initio* simulation package[22] which employs pseudopotentials, a plane-wave basis set, and periodic boundary conditions to determine the Kohn-Sham ground state. The exchange correlation functional is obtained using the generalized gradient approximation of Perdew and Wang.[23] We employ ultrasoft Vanderbilt-type pseudopotentials[24] with a core radii of 2.70 and 1.65 a.u. for Ti and N, respectively, and an energy cutoff of $E_{cut}=262$ eV for the plane-wave basis set expansion.

Typical calculation supercells contain 108 atoms in three layers with a 0.85-nm-thick vacuum layer. Equilibrium configurations are obtained by relaxing the ionic positions of adatoms and atoms in the surface layer using a conjugate-gradient algorithm. Subsurface atoms are fixed at their bulk positions. Calculations with larger supercells show that the maximum uncertainty in reported binding energies is $\simeq$0.8 eV. Binding and adsorption energies are defined with respect to free adspecies on the TiN(001) surface and free atoms or molecules in vacuum, respectively.

A variant of the nudged elastic band method is used to determine adatom surface diffusion paths.[25] For this purpose, adatoms are moved stepwise from an initial equilibrium position to a neighboring site with the same symmetry. At each step, the adatom and the first layer atoms are relaxed. Adatom relaxation is limited to a plane perpendicular to the path between initial and final positions while surface atom relaxation is unconstrained.

The adsorption energy E_{ad} and cluster binding energy E_B are defined as

$$E_{ad} = \tfrac{1}{2}\eta_N E_{N_2} + \eta_{Ti}E_{Ti} + E_s - E_{config} \qquad (1)$$

and

$$E_B = \eta_N E_{ad,N} + \eta_{Ti}E_{ad,Ti} - E_{ad,config}. \qquad (2)$$

E_{N_2} and E_{Ti} in Eq. (1) are the calculated total energies of an N_2 molecule and a Ti atom in vacuum, while η_{Ti} and η_N are the number of Ti and N adatoms considered in a given clus-

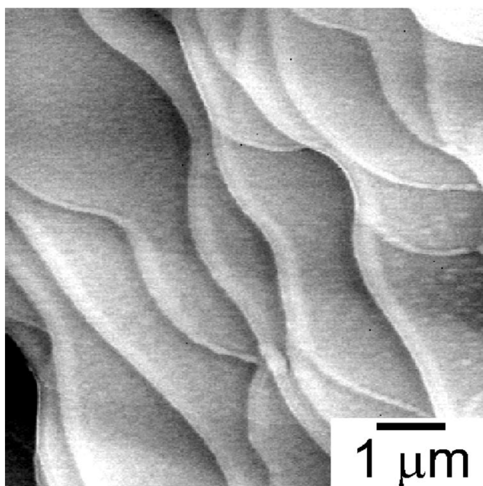

FIG. 1. An AFM image of a typical MgO(001) substrate surface following annealing at 1400 °C for 4 h in air. The image is $7 \times 7 \mu m^2$.

ter. E_s and E_{config} are the energies of the relaxed surface and the atomic configuration under investigation; $E_{ad,N}$, $E_{ad,Ti}$, and $E_{ad,config}$ in Eq. (2) are adsorption energies for single Ti and N atoms and for the cluster configuration. Binding energies defined by Eq. (2) are referenced to single adatoms and thus provide a measure of adatom-adatom bond strengths.

IV. RESULTS

An AFM image of a typical MgO(001) substrate following a 4 h anneal at 1400 °C in air is shown in Fig. 1. The substrate surface consists of large atomically flat terraces, with widths of $\simeq 1$ μm, separated by $\simeq$3-nm-high steps corresponding to approximately 15 atomic layers. The large terraces ensure that subsequent STM images of TiN(001) epitaxial overlayers are unaffected by substrate miscut or surface steps.

XRD ω-2θ scans from TiN/MgO(001) samples exhibit only one set of TiN peaks over the 2θ range between 20° and 80°. A typical scan is shown in Fig. 2(a). The peak, centered at 42.68° in excellent agreement with previous results for epitaxial TiN layers grown on MgO(001),[26] is indexed as the 002 Bragg reflection of B1-NaCl structure TiN while the 43.04° peak is due to 002 MgO.[33] XRD scans about the azimuthal angle ϕ, obtained in the parallel-beam mode with ω and 2θ angles optimized for the 113 peaks of MgO, contain four 90°-rotated 113 peaks at the same ϕ-angles for both MgO and TiN [Fig. 2(b)]. The combination of these results demonstrate that TiN layers grow epitaxially on MgO(001) with a cube-on-cube relationship: $(001)_{TiN} \| (001)_{MgO}$ and $[100]_{TiN} \| [100]_{MgO}$.

Figure 3 shows the results of temperature-dependant resistivity measurements for TiN(001) layers grown at 650, 850, and 950 °C. At low temperatures ($T < 40$ K), the resistivity $\rho(T)$ is constant and controlled by defect and impurity scattering. ρ increases approximately linearly with T at higher temperatures where the resistivity is primarily limited by phonon scattering. The room temperature resistivity $\rho_{300\ K}$ of layers grown at $T_s > 650$ °C is 13 $\mu\Omega$ cm and the 30 K value $\rho_{30\ K}$ is 0.45 and 0.73 $\mu\Omega$ cm for T_s=950 and 850 °C layers, respectively. Both $\rho_{300\ K}$ and the residual resistivity ratio, RRR=$\rho_{300\ K}/\rho_{30\ K}$ (RRR=29 with T_s =950 °C and 18 with T_s=850 °C), are equal to or better than the best values reported for TiN,[5] thus confirming the crystalline quality and purity of our samples. The room temperature resistivity of TiN(001) layers grown at T_s=650 °C is slightly higher $\rho_{300\ K}$=17.3 $\mu\Omega$ cm with RRR=4.4 indicative of a somewhat higher defect density at lower growth temperatures.

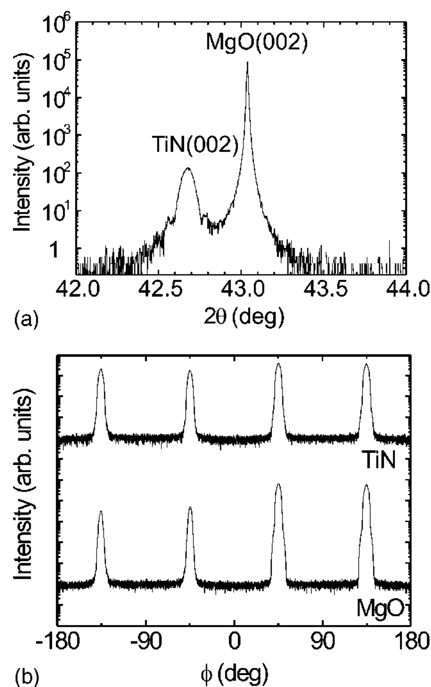

FIG. 2. XRD (a) (002)ω-2θ and (b) (113)φ scans of a 130-nm-thick TiN layer grown on MgO(001) at 1050 °C.

A typical STM image from an 8-nm-thick TiN(001) layer, grown on a TiN(001) buffer layer at 1050 °C and used to

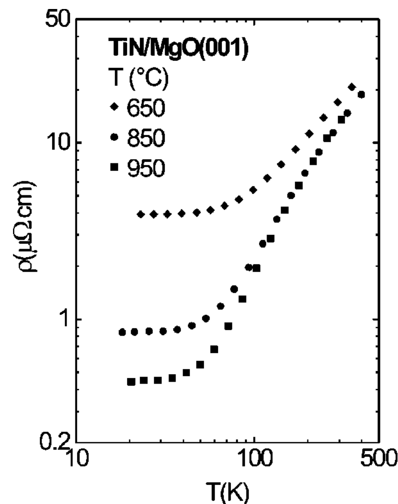

FIG. 3. The temperature-dependant resistivity of 130-nm-thick epitaxial TiN layers grown on MgO(001) with T_s=650 (squares), 850 (circles), and 950 °C (triangles).

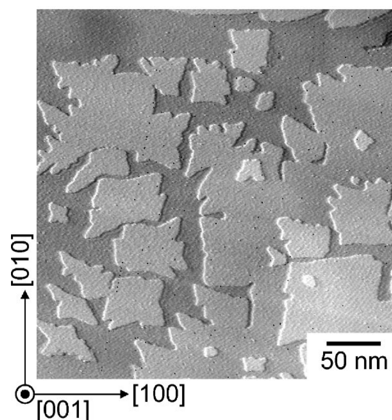

FIG. 4. An STM image of a TiN(001) surface used for investigating nucleation on a large terrace. The scan size is $340 \times 340\ \mathrm{nm}^2$.

determine nucleation lengths L_n on large terraces, is shown in Fig. 4. The TiN(001) surface consists of large atomically flat terraces, $\simeq 60$ nm wide, separated by 0.21-nm-high single-atom-height steps. While island edges are dendritic due to the relatively low growth temperature[27] [the melting temperature T_m for TiN is 2949 °C (Ref. 28)], they still exhibit the four-fold symmetry expected for TiN(001).[29]

STM images of samples for which 0.50 ± 0.60 ML of TiN was deposited on TiN(001) at (a) 510, (b) 600, and (c) 800 °C are shown in Figs. 5(a)–5(c). The partial monolayer deposition results in dendritic 2D islands with fractal-like step-edges, similar to those shown in Fig. 4. We measure the number density n of islands in step-free regions as a function of T_s. The nucleation length L_n is then determined from the relationship $L_n = 1/\sqrt{n}$. Using Fig. 5(b) as an example, there are 34 islands within a terrace area of $2600\ \mathrm{nm}^2$, resulting in a nucleation length of 8.7 nm at 600 °C. Several images are analyzed for each T_s value such that the total area over which we determine L_n includes >150 islands. Fig. 6 shows that L_n decreases exponentially with $1/T_s$, ranging from 17 nm at $T_s = 800$ °C to 6 nm at 510 °C. In these experiments, we limit our measurements to $T_s \leqslant 800$ °C in order to avoid L_n approaching the average terrace width, $\simeq 60$ nm.

Figure 7 consists of STM images from 8-nm-thick TiN(001) layers grown at (a) 650, (b) 720, and (c) 920 °C on TiN(001) buffer layers. These surfaces are typical of those from which we extract the characteristic island size R_c necessary to nucleate a new layer as a function of T_s. The 2D islands obtained at the lower temperatures, 650 and 720 °C, are dendritic, similar to those shown in Fig. 5, indicating that the activation energy for edge diffusion is sufficiently high to inhibit step edge relaxation. At the lowest temperature, $T_s = 650$ °C, the surface morphology is dominated by growth mounds formed due to kinetic roughening. The average mound spacing increases, and the height decreases with increasing T_s as evidenced by comparing, for example, Fig. 7(b), corresponding to $T_s = 750$ °C, to Fig. 7(a), $T_s = 650$ °C. Karr *et al.*[5] and Kodambaka *et al.*[30] have shown that TiN(001) has only a weak asymmetry in adatom attachment rates at step edges. For $T_s > 865$ °C, the TiN(001) homoepitaxial growth process approaches the layer-by-layer regime

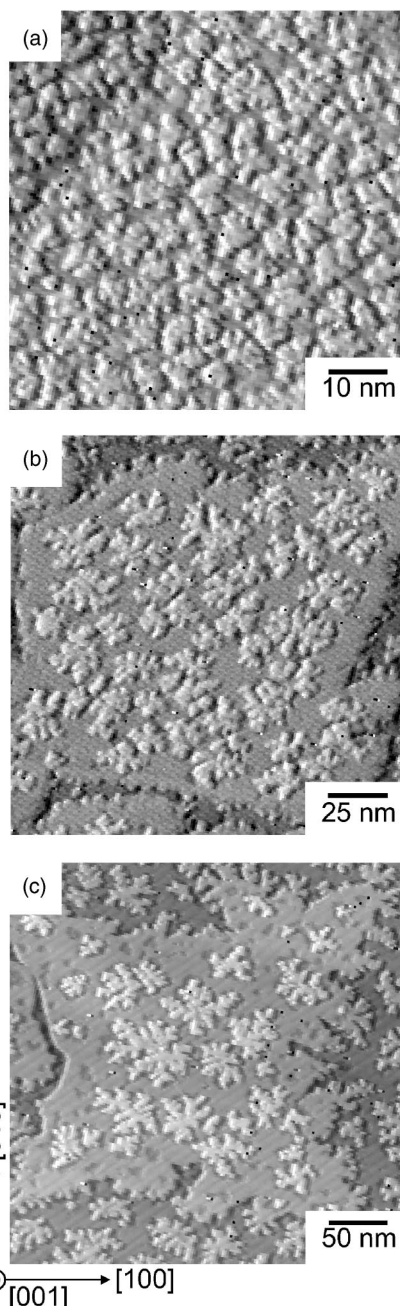

FIG. 5. STM images of 0.50 ± 0.06 ML TiN layers deposited at temperatures T_s on atomically flat TiN(001) terraces. Image sizes and deposition temperatures are: (a) $70 \times 70\ \mathrm{nm}^2$, $T_s = 510$ °C, (b) $170 \times 170\ \mathrm{nm}^2$, $T_s = 600$ °C, and (c) $200 \times 200\ \mathrm{nm}^2$, $T_s = 800$ °C.

and only two to three layers are visible in STM images. Islands deposited at 920 °C, while still dendritic, exhibit fourfold symmetry.

In addition to the growth mounds, surface steps produced by plastic deformation of the TiN(001) layer, i.e., "slip-steps," are visible in the image from the 720 °C sample in Fig. 7(b). However, the fact that the island morphologies are continuous from one side of a slip-step to the other indicates that dislocation formation occurs while the sample cools following growth.[18] A slip-step formed during growth would

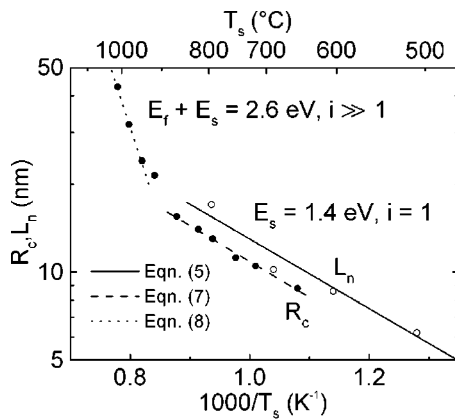

FIG. 6. The solid data points (dashed lines) correspond to the characteristic TiN(001) island size R_c required for nucleation of an upper layer while the open data points (solid line) are the measured TiN(001) nucleation lengths L_n on large open terraces as a function of the deposition temperature T_s.

quickly become indistinct due to the repeated nucleation and growth of new terraces.

The formation of slip-steps following deposition can be explained by an increase in the compressive film stress during cooling: The differential thermal expansion of MgO (Ref. 31) is ≃0.3% larger than that of TiN (Ref. 32) between 720 °C and room temperature. The biaxial compressive strain at 720 °C, as a function of the room temperature lattice constants ($a_{\mathrm{TiN}}=0.4240$ nm and $a_{\mathrm{MgO}}=0.42112$ nm),[33] is $\varepsilon=(a_{\mathrm{TiN}}-a_{\mathrm{MgO}})/a_{\mathrm{MgO}}-0.004=1.8\times10^{-3}$. The critical thickness for the introduction of misfit dislocations in TiN layers grown on MgO(001), estimated based upon the model of Matthews and Blakeslee,[34] is ≃60 nm at 720 °C and ≃12 nm at room temperature. Since the total film thickness, including the buffer layers, in these samples is 60 nm, many STM images exhibit slip-steps due to misfit dislocation propagation during cooling.

The characteristic island size R_c required to nucleate a layer is primarily dependant on the smallest island dimension since adatom diffusion is isotropic on a square lattice. Figure 7(c) shows two islands with inscribed ellipses representing the island size R, where we define R as one-half the minor axis of the largest ellipse which fits within the rough step edges of the island. The larger island in Fig. 7(c) exhibits nucleation of a layer, while the smaller island does not.

Based upon the analytical model of Tersoff *et al.*,[2] R is related to R_c through the expression

$$f=1-\exp\left[-\left(\frac{R}{R_c}\right)^8\right], \tag{3}$$

where f is the fraction of islands of size R which exhibit second-layer nucleation. We measure both R and $f(R)$ for >100 islands at each growth temperature and calculate R_c by applying Eq. (3) which was derived for the case corresponding to weak adatom attachment asymmetry at ascending versus descending steps, circular islands, and a stable cluster size of two adatoms (i.e., $i=1$). The second assumption clearly does not apply here and the validity of the third assumption depends upon T_s. However, since we are only using Eq. (3) to systematically obtain R_c, the assumptions are not critical and only lead to a maximum uncertainty, primarily due to island shape anisotropy, in determining R_c of ±10%. Changing the value of i increases the rate of change

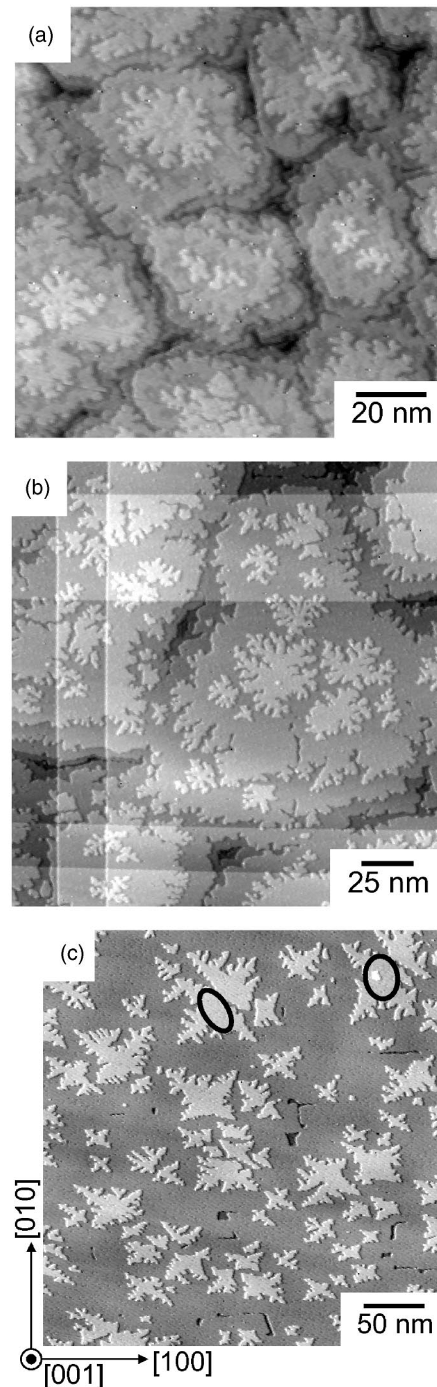

FIG. 7. STM images of the surface of 8-nm-thick TiN(001) layers grown at temperatures T_s on a two-step buffer layer consisting of 20 nm TiN(001) deposited at 650 °C and 40 nm at 750 °C. Image sizes and deposition temperatures are (a) 110×110 nm^2, $T_s=650$ °C, (b) 210×210 nm^2, $T_s=720$ °C, and (c) 340×340 nm^2, $T_s=920$°C.

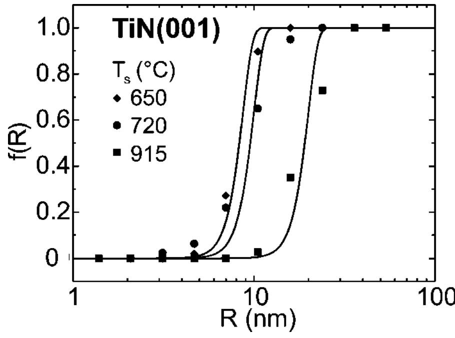

FIG. 8. The fraction f of TiN(001) islands of size R on which a cluster has nucleated during epitaxial TiN growth at T_s=650, 720, and 915 °C.

in $f(R)$, but has a negligible effect on the value of R_c we extract.

Figure 8 shows typical $f(R)$ versus R data sets at 650, 720, and 915 °C together with the fits obtained using Eq. (3). Extracted R_c values are plotted for all film growth temperatures T_s in Fig. 5. Two temperature regimes are clearly apparent: one ranging from 650 to 865 °C, and the other from 910 to 1010 °C. The transition between these regimes is due to a temperature-dependant change in the size of the smallest stable cluster as discussed below in Sec. V. The temperature range over which we measure R_c is limited to $T_s > 650$ °C since lower temperature layers are highly defective, as evidenced by an increase in the low temperature resistivity.[35]

R_c in Fig. 5 increases from 9 nm with T_s=650 °C to 16 nm at 865 °C. Further increases in T_s result in R_c increasing at a higher rate, ranging from 21 nm with T_s=910 °C to 43 nm at T_s=1010 °C. We limit our measurements of R_c to $T_s \leqslant 1010$ °C due to the onset of Ca out-diffusion from the MgO substrate as shown by Auger electron spectroscopy.

V. DISCUSSION

The island nucleation length L_n on large terraces is a function of the activation energy E_s for surface diffusion and the binding energy E_b of small unstable clusters on the surface. We define E_b as the difference in energy between the bound cluster and the constituent adspecies existing free on the surface. From nucleation rate theory[4]

$$L_n = \frac{1}{\sqrt{0.2}}\left(\frac{\nu a^2}{F}\right)^{i/(2i+4)} \exp\left(\frac{-(iE_s+E_b)}{(2i+4)kT_s}\right), \tag{4}$$

where ν is a pre-exponential frequency factor, a^2 is the size of a surface unit cell, F is the deposition flux, and i is defined as the size of the largest unstable cluster, often called the critical cluster.

Island nucleation occurs when $(i+1)$ mobile adspecies encounter each other and form a stable cluster. Since the temperatures, 510 to 800 °C, over which we have measured L_n on TiN(001) are low with respect to the TiN melting point T_m ($T_s/T_m \simeq 0.24$ to 0.33),[27] we expect that the smallest stable cluster is two adspecies (i.e., $i=1$) and, hence, the nucleation process is diffusion limited. In this case, Eq. (4) becomes

$$L_n = \frac{1}{\sqrt{0.2}}\left[\frac{\nu a^2}{F}\exp\left(\frac{-E_s}{kT_s}\right)\right]^{1/6}. \tag{5}$$

From the temperature-dependant L_n data shown in Fig. 6, a least-squares fit using Eq. (5) results in a surface diffusion activation energy $E_s = 1.4 \pm 0.1$ eV with a frequency prefactor $\nu = 10^{13\pm1}$ s^{-1}.

As a parallel approach to extracting the characteristic length scale for homoepitaxial nucleation on TiN(001), we measure the characteristic island size R_c necessary to nucleate a layer. Figure 6 is a plot of R_c as a function of T_s; the increase in slope at $T_s > 865$ °C is due to an increase in the size of the smallest stable cluster. Tersoff *et al.*[2] model nucleation on a growing island to derive an expression for R_c as a function of L_n, E_s, and the binding energy E_b of small clusters. Based upon our experimental results in Fig. 6, we set $L_n \simeq R_c$. Since TiN(001) is known to have only a weak asymmetry in adatom attachment rates at ascending versus descending steps,[5,30] the characteristic island size is given by[2]

$$R_c = \left(\frac{4(i+2)(i+3)}{\pi}4^i\right)^{i/(2i+4)}\left(\frac{\nu a^2}{F}\right)^{i/(2i+4)} \exp\left(\frac{-(iE_s+E_b)}{(2i+4)kT_s}\right). \tag{6}$$

The low temperature regime, 650 to 865 °C, corresponds approximately to the temperature range over which we measured L_n and for which we previously argued that the nucleation process is diffusion limited ($i=1$). In this case, Eq. (6) reduces to

$$R_c = \left(\frac{192}{\pi}\right)^{1/6}\left[\frac{\nu a^2}{F}\exp\left(\frac{-E_s}{kT_s}\right)\right]^{1/6}. \tag{7}$$

A least-squares fit of the $R_c(T_s)$ data between 650 and 865 °C in Fig. 6 yields $E_s = 1.4 \pm 0.1$ eV with $\nu = 10^{13\pm1}$ s^{-1} for nucleation on growing islands, in agreement with the results given above for nucleation on large terraces.

Identifying the primary diffusing species is fundamental to understanding the atomic processes occurring during nucleation. For TiN(001), there are several possible candidates including Ti and N adatoms and $TiN_x (x=1,2,3,\ldots,)$ admolecules. To probe the nature of the primary diffusing species, we use *ab initio* density functional theory (DFT) to calculate the adsorption, diffusion, and binding energies of adatoms and small clusters on TiN(001). A comparison of our experimentally determined diffusion energy with the DFT results allows us to isolate potential rate-controlling surface species.

The lowest-energy migration path for an itinerant Ti adatom on TiN(001) is illustrated in Fig. 9(a).[12] The adatom, starting from its stable fourfold-hollow site (labeled A) with an adsorption energy E_{ad} of 3.30 eV, moves along the $\langle 110 \rangle$ directions through a metastable site B, where E_{ad}=3.01 eV, above a N atom to the next stable site C. The two potential-energy saddle points are approximately equidistant between sites A/B and B/C. E_{ad} is 2.95 eV at the saddle points, resulting in an activation energy E_s of 0.35 eV for Ti surface

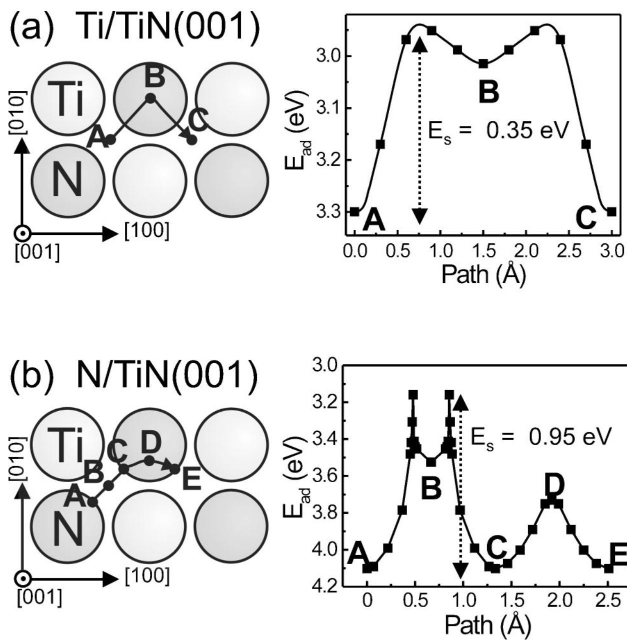

FIG. 9. Low energy diffusion paths and corresponding plots of the adsorption energy E_{ad} versus position along the migration path of (a) Ti and (b) N adatoms on TiN(001) as obtained from density functional theory calculations.

diffusion on TiN(001). This is a factor of four smaller than that measured by experiment. Thus, we conclude that Ti is not the primary diffusing species.

Petrov *et al.*[36] have shown there is a significant flux of atomic N (including N_2^+ ions which dissociate upon colliding with the surface) incident at the growing film surface during reactive magnetron sputter deposition of TiN in pure N_2. The calculated lowest-energy migration path of a N adatom on TiN(001) is shown in Fig. 9(b).[21] Like Ti, the initial N motion is in the $\langle 110\rangle$ direction, starting from a stable position A(E_{ad}=4.1 eV) where it is bonded to a N atom beneath it. The N adatom moves through position B, a metastable fourfold hollow site (E_{ad}=3.5 eV), to a stable site C. The sharp peaks in the plot of E_{ad} versus distance along the pathway from A to B and B to C correspond to energy barriers of 0.95 eV for breaking and forming bonds with underlying N atoms at a lateral distance of 0.48 Å from the stable sites A and C. The peaks in E_d along the path A-C in Fig. 9(b) appear steep since the abscissa of the plot represents the path of the adatom and rearrangements of atoms below the adatom result in large changes in the binding energy with correspondingly small adatom movements. For example, the underlying N which is initially bonded to the diffusing N adatom, is displaced by up to 0.34 Å, then relaxes following bond breaking to approximately its original position.

As N adatoms diffuse and encounter each other on TiN(001), N_2 forms with a binding energy of 2.1 eV and an adsorption energy of only 0.2 eV with respect to free N_2. Therefore, N_2 desorbs at near kinetic rates from TiN(001) at the growth temperatures T_s used for our experiments (>500 °C). We conclude that N is not the primary diffusing species since the calculated diffusion energy 0.95 eV is significantly smaller than the diffusion activation energy 1.4 eV we obtain experimentally.

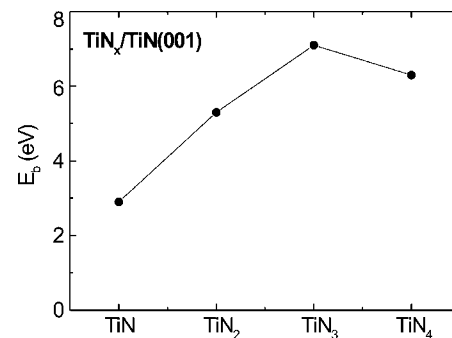

FIG. 10. Binding energies E_b, obtained from density functional theory calculations, of TiN_x admolecules on TiN(001).

Based upon the above results, we propose that TiN_x admolecules are the primary diffusing species during reactive magnetron sputtering in pure N_2. Calculated admolecule binding energies E_b for TiN_x (x=1,2,3, and 4) referenced to the constituents existing free on TiN(001) are plotted in Fig. 10. E_b increases from 2.7 eV with x=1 to 6.8 eV with x=3, then decreases to 5.9 eV for TiN_4. The stability of individual TiN_x($x\geq 2$) admolecules to N_2 detachment on TiN(001) was also investigated using DFT calculations. We find that TiN_4 dissociation to TiN_2 and N_2 adspecies decreases the system energy by 0.91 eV while N_2 dissociation from TiN_3 and TiN_2 increases the total energy by 2.29 and 3.33 eV, respectively. Consequently, for film growth under high-N-supply-rate conditions, as in the present experiments, TiN_2 and/or TiN_3 are expected to constitute the majority of free TiN_x admolecules and are therefore, the primary diffusing species. Reducing the atomic N supply rate will increase the coverages of Ti and TiN adspecies, while decreasing TiN_2 and TiN_3 coverages, leading to a change in the nucleation kinetics.

At $T_s\geq 865$ °C, Fig. 6 shows a dramatic increase in the rate of change of R_c with T_s. There are two possible explanations for this behavior, either a change in the nature of the primary diffusing species or an increase in the critical cluster size. If we assume that the critical cluster size remains constant, the diffusion activation energy we extract is 8.4 eV. However, this is larger than all TiN_x admolecule adsorption energies on TiN(001), and thus not physically reasonable. We therefore conclude that there is an increase in the largest unstable cluster size (i.e., $i>1$) at $T_s>865$ °C. The data in Fig. 6 indicates that i initially increases over the T_s range between 865 and 945 °C. For $T_s\geq 945$ °C, where we obtain a linear relationship between $\ln(R_c)$ and $1/T_s$, the data is well fit for all $i\geq 1$, for which R_c is given by[2]

$$R_c = 2\left[\frac{a^2\nu}{F}\exp\left(\frac{-(\mathrm{E}_s+\mathrm{E}_f)}{kT_s}\right)\right]^{1/2}, \qquad (8)$$

where we have defined the formation energy E_f as E_b/i. A least-squares fit of Eq. (6) to the data in Fig. 6 for $945<T_s\leq 1010$ °C results in $(E_s+E_f)=2.6\pm0.2$ eV with $\nu=10^{13\pm1}\,\mathrm{s}^{-1}$. Assuming that the nature of the primary diffusing species is independent of T_s over the temperature range

of these experiments, E_s remains constant at 1.4 ± 0.1 eV with $E_f = 1.2 \pm 0.2$ eV.

VI. CONCLUSIONS

In situ UHV-STM experiments, *ab initio* calculations, and analytical theory have provided atomic-scale insights into the kinetics which govern nucleation of TiN on TiN(001) during reactive magnetron sputter deposition in pure N_2. Excellent agreement is obtained between nucleation measurements on both large terraces and growing islands. Over the growth temperature range $500 \leqslant T_s \leqslant 865\,^{\circ}\mathrm{C}$, we find that nucleation is diffusion limited with $i=1$ and obtain a diffusion activation energy of 1.4 ± 0.1 eV with a prefactor of $10^{13\pm1}$ s^{-1}. At higher growth temperatures, nucleation becomes limited by the formation rate of stable clusters and we obtain a value of 2.6 ± 0.2 eV for the sum of the surface diffusion and admolecule formation E_f energies where $E_f = 1.2 \pm 0.2$ eV. Comparison of *ab initio* calculations with experimental results show that TiN_x is the primary diffusing species. During deposition of TiN on TiN(001) in the presence of a large atomic N flux incident at the growing film, as is the case for the present experiments utilizing reactive magnetron sputter deposition in pure N_2, we find that the primary diffusing species are TiN_2 and/or TiN_3 admolecules. We expect that a significant decrease in the atomic N flux achieved through, for example, deposition in mixed Ar/N_2 discharges, will lead to an increase in the steady-state Ti and TiN coverages with a corresponding decrease in TiN_2 and TiN_3 admolecule coverages and, hence, result in a change in nucleation kinetics.

ACKNOWLEDGMENTS

The authors gratefully acknowledge the financial support of the U.S. Department of Energy, Division of Materials Science, under Grant No. DEFG02-91ER45439 through the University of Illinois Frederick Seitz Materials Research Laboratory (MRL) and the Division of Materials Research, National Science Foundation. We also appreciate the use of the facilities in the Center for Microanalysis of Materials, partially supported by DOE, and the FS-MRL.

[1] S. Stoyanov and I. Markov, Surf. Sci. **116**, 313 (1982).
[2] J. Tersoff, A. W. Denier van der Gon, and R. M. Tromp, Phys. Rev. Lett. **72**, 266 (1994).
[3] D. Walton, J. Chem. Phys. **37**, 2182 (1962).
[4] J. A. Venables, Philos. Mag. **27**, 693 (1973).
[5] B. W. Karr, D. G. Cahill, I. Petrov, and J. E. Greene, Phys. Rev. B **61**, 16 137 (2000).
[6] W. Theis and R. M. Tromp, Phys. Rev. Lett. **76**, 2770 (1996).
[7] B. Fischer, H. Brune, J. V. Barth, A. Fricke, and K. Kern, Phys. Rev. Lett. **82**, 1732 (1999).
[8] M. Bott, M. Hohage, M. Morgenstern, T. Michely, and G. Comsa, Phys. Rev. Lett. **76**, 1304 (1996).
[9] K. Fischer and H. Oettel, Surf. Coat. Technol. **97**, 308 (1997).
[10] P. V. Kola, S. Daniels, D. C. Cameron, and M. S. J. Hashmi, J. Mater. Process. Technol. **56**, 422 (1996).
[11] M. Zlatanovic, D. Sesum, Dj. Djukic, and N. Popovic, Mater. Sci. Forum **282–283**, 139 (1998).
[12] J. Baumann, T. Werner, A. Ehrlich, M. Rennau, Ch. Kaufmann, and T. Gessner, Microelectron. Eng. **37–38**, 221 (1997).
[13] J.-S. Chun, P. Desjardins, C. Lavoie, I. Petrov, C. Cabral, Jr., and J. E. Greene, J. Vac. Sci. Technol. A **19**, 2207 (2001).
[14] J.-S. Chun, J. R. A. Carlsson, P. Desjardins, D. B. Bergstrom, I. Petrov, J. E. Greene, C. Lavoie, C. Cabral, Jr., and L. Hultman, J. Vac. Sci. Technol. A **19**, 182 (2001).
[15] F. Adibi, I. Petrov, J. E. Greene, L. Hultman, and J.-E. Sundgren, J. Appl. Phys. **73**, 8580 (1993).
[16] J. E. Greene, J.-E. Sundgren, L. Hultman, I. Petrov, and D. B. Bergstrom, Appl. Phys. Lett. **67**, 2928 (1995).
[17] G. Ehrlich and F. G. Hudda, J. Chem. Phys. **44**, 1039 (1966).
[18] B. W. Karr, I. Petrov, D. G. Cahill, and J. E. Greene, Appl. Phys. Lett. **70**, 1703 (1997).
[19] Y.-W. Kim, I. Petrov, H. Ito, and J. E. Greene, J. Vac. Sci. Technol. A **13**, 2836 (1995).
[20] L. Hultman, S. A. Barnett, J.-E. Sundgren, and J. E. Greene, J. Cryst. Growth **92**, 639 (1988).
[21] D. Gall, S. Kodambaka, M. A. Wall, I. Petrov, and J. E. Greene, J. Appl. Phys. **93**, 9086 (2003).
[22] G. Kresse and J. Hafner, Phys. Rev. B **47**, 558 (1993); **49**, 14 251 (1994); G. Kresse and J. Furthmüller, Comput. Mater. Sci. **6**, 15 (1996); Phys. Rev. B **54**, 11 169 (1996).
[23] J. P. Perdew and Y. Wang, Phys. Rev. B **45**, 13 244 (1992).
[24] D. Vanderbilt, Phys. Rev. B **41**, 7892 (1990); G. Kresse and J. Hafner, J. Phys.: Condens. Matter **6**, 8245 (1994).
[25] G. Mills, H. Jónsson, and G. K. Schenter, Surf. Sci. **324**, 305 (1995).
[26] J.-S. Chun, J. R. A. Carlsson, P. Desjardins, D. B. Bergstrom, I. Petrov, J. E. Greene, C. Lavoie, C. Cabral, and L. Hultman, J. Vac. Sci. Technol. A **19**, 182 (2001).
[27] 1050 °C (1323 K), the highest temperature at which we deposit TiN, corresponds to a homologous temperature T_s/T_m of 0.41 where $T_m = 3222$ K is melting point of TiN.
[28] L. E. Toth, *Transition Metal Carbides and Nitrides* (Academic, New York, 1971), p. 5.
[29] S. Kodambaka, V. Petrova, S. V. Khare, A. Vailionis, I. Petrov, and J. E. Greene, Surf. Sci. **513**, 468 (2002).
[30] S. Kodamabaka, V. Petrova, A. Vailionis, I. Petrov, and J. E. Greene, Surf. Sci. **526**, 85 (2003).
[31] J. B. Austin, J. Am. Ceram. Soc. **14**, 795 (1931).
[32] K. Aigner, W. Lengauer, D. Rafaja, and P. Ettmayer, J. Alloys Compd. **215**, 121 (1994).
[33] R. W. G. Wyckoff, *Structures* (Wiley, New York, 1963), Vol. 1, p. 88.
[34] J. W. Matthews and A. E. Blakeslee, J. Cryst. Growth **27**, 118 (1974).
[35] L. Hultman, G. Hånkansson, U. Wahlström, J.-E. Sundgren, I. Petrov, F. Adibi, and J. E. Greene, Thin Solid Films **205**, 153 (1991).
[36] I. Petrov, A. Myers, J. E. Greene, and J. R. Abelson, J. Vac. Sci. Technol. A **12**, 2846 (1994).